Micro-PL analysis of high current density resonant tunnelling diodes for THz applications

M.Cito[1], D. Cimbri[1], D. Childs[1], R. Baba [1], B. A. Harrison[2], A. Watt[1], T. Mukai[3], E. Wasige[1] and R.A. Hogg[1]

AFFILIATIONS

1. School of Engineering, University of Glasgow, Oakfield Avenue, G12 8LT Glasgow, United Kingdom
2. EPSRC National Centre for III-V Technologies, Department of Electronic & Electrical Engineering, University of Sheffield, North Campus, Broad Lane, Sheffield S37HQ, United Kingdom
3. Sensing Technology R&D Project, R&D Headquarters LED Division, RohmCo.Ltd., 21 Saiin Mizosaki-cho, Ukyo-ku, Kyoto 615-8585, Japan

Author to whom correspondence should be addressed: michele.cito.res@gmail.com

ABSTRACT

Low-temperature micro-photoluminescence (µPL) is used to evaluate wafer structural uniformity of current densities >5mA/µm^2 InGaAs/AlAs/InP resonant tunnelling diode (RTD) structures on different length scales. Thin, highly strained quantum wells (QWs) are subject to monolayer fluctuations, leading to a large statistical distribution in their electrical properties. This has an important impact on the RTD device performance and manufacturability. The PL spot size is reduced using a common photolithography mask to reach a typical high J_{peak} for a given RTD mesa size (1 ~ 100 µm^2). We observe that for lower strain-budget samples, that the PL line-shape is essentially identical for all excitation/collection areas. For higher strain-budget samples, there is a variation in the PL line-shape that is discussed in terms of a variation in long-range disorder brought about by strain relaxation processes. The RTD operating characteristics are discussed in light of these findings, and we conclude that strain model limits overestimate the strain budget that can be incorporated in these devices. We also highlight µPL as a powerful non-destructive characterization method for RTD structures.

There is a lack of efficient high-speed technology able to satisfy the ever-growing wireless data-demand [1, 2]. As a consequence, the THz frequency range (0.1-10THz)[3] has attracted considerable interest as it offers the wide bandwidth required for high data-rate communications. Resonant tunneling diodes (RTDs) have been demonstrated to be the fastest solid-state device with oscillation near 2 THz [4] with highly attractive characteristics: tunability, compact dimensions, and room temperature operation [5] .

As for all quantum-effect devices [6], the RTD performance is critically dependent on crystal purity and heterointerface perfection. We previously demonstrated how ~80% of the parasitic valley current is associated with non-thermal inelastic scattering [7], and as a consequence, the RTD output power is limited by crystal-related imperfections.

RTDs are composed of a single double-barrier QW generally growth by molecular beam epitaxy (MBE) or metal-organic vapor-phase epitaxy (MOVPE), despite the outstanding precision offered by these technologies, wafer characterization remains a difficult process, leading to knowledge barriers in

epitaxial process optimisation. X-ray diffraction characterization provides limited information compared to a periodic QW superlattice [8], whilst photoluminescence techniques are uninformative at room temperature [9].

The electrical and physical characterization of these structures is therefore important to improve upon the reproducibility and support device engineering and commercialization. We previously proposed a non-destructive characterization scheme based on low-temperature photoluminescence spectroscopy (PL) in combination with high-resolution X-ray diffraction (HD-XRD), improved by the inclusion of a buried undoped "copy" QW [8]. Critical information on the band offset has subsequently been obtained by applying photoluminescence excitation spectroscopy (PLE) with the additional benefit of an overall improvement in the repeatability of the realised epitaxial structure [10]. It is important to note that several important non-destructive characterisation techniques perform significant spatial-measurement averaging of a sample. Given the mesoscopic nature of RTDs, the relevance of these techniques is questionable, or can be improved upon.

In this paper, we investigate the use of micro-PL to evaluate structural perfection on different length scales (higher and lower than the exciton radius) in two high current density RTD structures with highly-strained QWs growth by MOVPE. The PL spot size is progressively reduced, reaching the typical RTD mesa-size (a few square microns). This is accomplished by employing windows (holes) of a reducing area on a chromium photolithography mask mounted on top of the wafer. We observed PL line-shape differences between low and high strain-budget samples, highlighting the presence of long-range structural disorder associated with the strain relaxation process. The I-V characteristics of RTDs fabricated from these wafers are analysed as a function of mesa-size, with the low strain-budget sample showing poor scaling of both peak and valley current with area, in line with our non-destructive measurements of structural imperfection. This direct correlation of variation in micro-PL line shapes, and variation of the static I-V characteristics indicates that care is needed in using macroscopic LT-PL for epitaxial wafer validation, and that micro-PL provides a powerful technique in assessing the quality of RTD epitaxial materials.

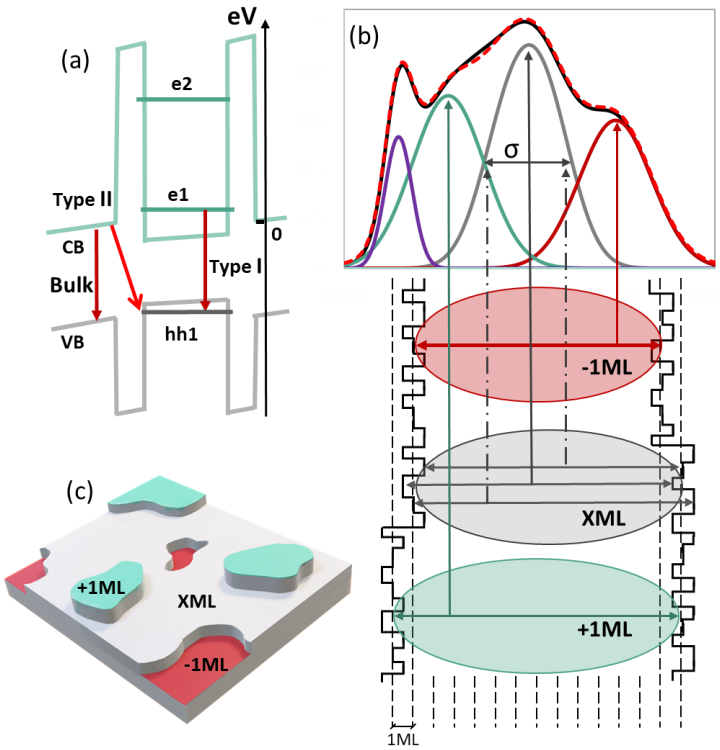

Figure 1 Schematic representation of the (a) QW band-profile and optical transitions detected by PL. (b) AlAs barriers roughness, the well thickness, and their impact on the PL spectra. Vertical dashed lines indicate the thickness in atomic monolayers (1 ML ~2.93 Å), horizontal coloured arrows correspond to local ML fluctuations, -1ML (red), +1ML (green) and the designed thickness (grey). Representative deconvoluted PL spectra illustrate the origin of the transition broadening (see text). (c) 3D-pictogram of the in-plane extension of the ML fluctuations, in the same colours of (b).

Figure 1(a) shows a schematic of the band-profile, with lines indicating the first quasi-bound state (e_1) in the QW conduction band, and the first heavy hole state (hh_1) in the valence band. Red arrows indicate the optical transition detectable in PL. The bulk transition is due to the LM-InGaAs bulk bandgap, the Type-II transition is generated by the recombination of electrons in the bulk conduction band with the heavy hole state in the QW, the Type-I transition is due to the optical transition between the quasi-bound states in the active region, from e_1 to hh_1.

Figure 1(b) shows a not-to-scale schematic of the RTD active-region, with the black lines highlighting the heterointerface roughness between the AlAs barrier and the InGaAs well. Vertical black dashed-lines indicate the thickness in ML units while the horizontal arrows indicate the monolayer fluctuation in the well thickness, designated as XML in grey, the -1ML in dark red and the +1ML in green. Figure1(b) shows schematically the impact of these growth imperfections on the PL spectra, the interface roughness (length scale<<exciton) creates broadened peaks (increase in σ) while the ML fluctuation creates separate features (length scale>>exciton), leading to an overall broad PL spectrum [11]. Coloured ellipses indicate the QW excitons (radius ~10nm [12]), which act as our probe, highlighting the length-scale of these structural imperfections [13]. Figure1 (c) shows a representative wafer slice where the ML-islands are highlighted using the same colour coding from figure1(b). As a point of reference, a scanning Cathodoluminescence (CL) study on the GaAs/AlGaAs material system showed the ad-extension of these islands to be >2um^2 [14]. For the InGaAs/InP material system under high strain conditions ([In] ≥ 80%), similar results were observed by scanning tunnelling microscopy (STM) [15] and atomic force microscopy (ATM) [16]. Typical RTD mesa sizes vary with application, ranging from 25µm^2 for Sub-THz oscillators [17] to ~1um^2 for high Jpeak structures for high-frequency

operation [5, 18]. For such structures, the device/mesa dimensions are comparable with the expected extension of ML-islands.

Structures were grown using a Thomas Swan 7x2 robot-loaded close-coupled showerhead (CCS), metal-organic vapour phase (MOVPE) reactor. The group III precursors were trimethylalluminium (TMA), trimethylgallium (TMG) and trimethylindium (TMI), whilst the group V precursors were arsine (AsH_3) and phosphine (PH_3). A 300nm InP buffer was deposited at 580°C on Fe doped InP (001) offcut by 0.1 degrees towards (111). The rest of the structures were grown at 595°C. 200nm of AlInAs was grown to getter oxygen and improve the AlAs barrier symmetry, whilst 25nm of InGaAs was grown to aid the nucleation of the AlInAs. A CP21 wet etch profiler and Hall measurements were used to calibrate the doping concentrations and the layer compositions were calibrated using a Bruker D8 Discovery.

After the InP buffer, the overgrowth continues with 200 nm undoped $In_{0.53}Ga_{0.47}As$. 400 nm highly n-doped $In_{0.53}Ga_{0.47}As$ ($2x10^{19}$ cm^{-3} Si) is then grown for the lower contact. A 20 nm n-doped $In_{0.53}Ga_{0.47}As$ ($3x10^{18}$ cm^{-3} Si) emitter layer is then deposited, followed by a 2 nm $In_{0.53}Ga_{0.47}As$ spacer layer. An InGaAs quantum well is formed between two 1.1 nm AlAs barriers. On the collector side, a 20 nm $In_{0.53}Ga_{0.47}As$ spacer layer is grown with a 25 nm $In_{0.53}Ga_{0.47}As$ ($3x10^{18}$ cm^{-3} Si) collector layer. The epitaxy is terminated with 15 nm n-doped $In_{0.53}Ga_{0.47}As$ ($2x10^{19}$ cm^{-3} Si), and 8 nm $In_{0.80}Ga_{0.20}As$ ($2x10^{19}$ cm^{-3} Si). The two samples analysed in this paper differ only by the QW characteristics, the first one has 12 ML of InGaAs with a mole fraction of 85%, the second one has 16ML with a mole fraction of 80%, samples will be denoted as sample “A” and “B” respectively.

Low-temperature PL was performed in a closed-cycle helium cryostat, with the sample at a temperature of 13K. A frequency-doubled neodymium-doped yttrium-vanadium-oxide (Nd:YVO4) laser at 532 nm was used to excite the sample. The PL signal was filtered by a double-grating Bentham DMc150 monochromator and detected by an InGaAs trans-impedance photodetector. Measurements were conducted using a laser power density of ~0.5 $mWcm^{-2}$ with the photomask varying the excitation/detection spot size. The mask is a common commercial 3”x3”x0.006” chrome/quarts photolithography mask, positioned with the chrome absorber in contact with the sample. The designed pattern has 19 different holes, with dimensions providing areas from 100 μm^2 to 10 μm^2 (step of 10 μm^2) and from 9 μm^2 to 1 μm^2 (step of 1 μm^2). Each element in the pattern is separated by

300 µm to avoid PL-contribution from more than one source. The overall pattern covers an area lower than 1 cm^2.

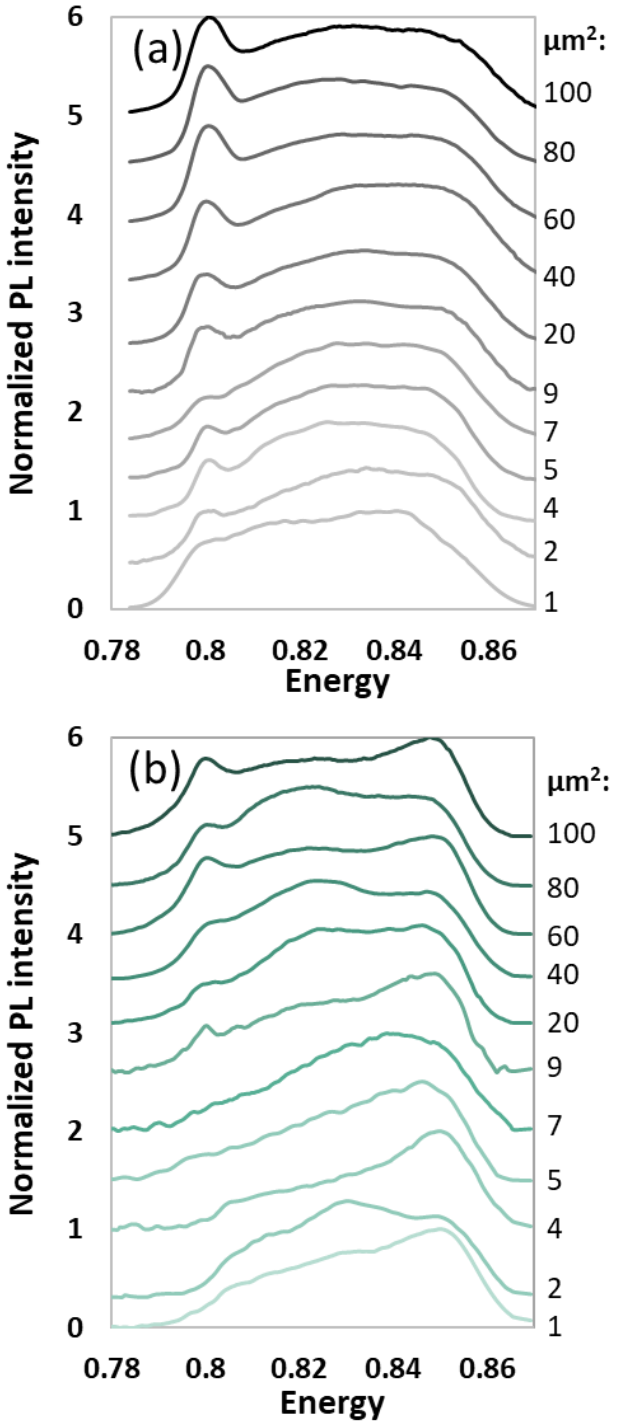

Figure 2 Experimental PL data from sample-A (a) and sample-B (b) reducing the laser spot-size, with the corresponding window dimension reported on the right-side. Spectral data normalised and offset for presentation purposes.

Figure 2(a&b) shows the experimental low-temperature PL spectra from samples-A&B, respectively. Data are normalized and shifted in amplitude and the curves are disposed in decreasing order starting from the top 100 μm^2 holes. In both series of spectra, we observe a peak at 0.8 eV associated with the LM-InGaAs bulk peak, at higher energy the spectra is broad due to the three Type-I transitions as explained in Figure 1(b).

Figure 2(a) shows that with reducing mask area, essentially identical spectra are obtained. The dominance of the bulk transition is observed to reduce with reducing holes size, but down to a 4 μm^2 hole size the contribution of X, +1ML and –1ML Type-I PL transitions remains almost unchanged. For the smallest holes used, small changes in the intensity of the X, +1ML and –1ML Type-I PL transitions are observed. Figure2(b) shows the dominance of the bulk transition is again observed to reduce with reducing mask size, but quite different PL spectra (different contributions of X, +1ML and –1ML Type-I transitions) are obtained for all hole sizes.

The length scale of long-range disorder (>>exciton) is therefore observed to be quite different in these two samples. For sample-A, this is ~4 μm^2, whilst for sample-B it is ~>100 μm^2. The growth conditions for the two samples were nominally identical and therefore these differences in PL (and hence structural uniformity) are attributed to the structural design itself. The active regions are highly strained, which is known to lead to corrugation of the growth plane prior to defect formation [19]. For the coherent growth of strained structures without the formation of dislocations, the limit has often been described in term of the *critical thickness,* defined as the maximum achievable thickness of a material X pseudomorphically grown on material Y [20]. One of the more realistic limits was modelled using a mechanical equilibrium approach by Matthews & Blakeslee (M&B) [19]. This model was investigated for the AlAs/InGaAs/InP material system [21] to design highly-strained QWs and for the optimization of the intrinsic resonator efficiency in high-current-density RTD designs.

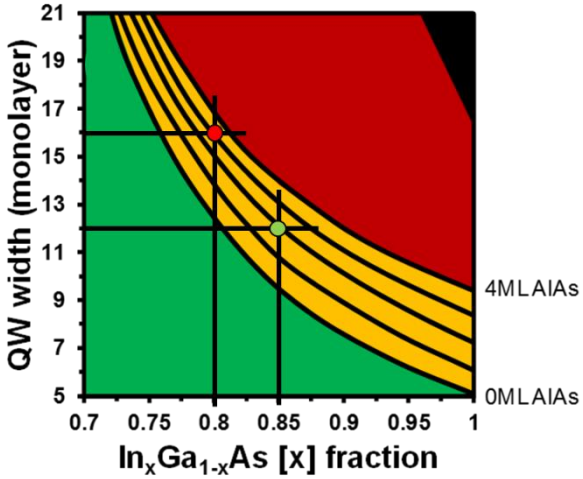

Figure 3 Modelled schematic of the critical thickness limits for QW width and crystalline alloy mole fractions, where x=0.532 is lattice-matched to InP, used with permission after[21] . The green zone indicates uniform growth, yellow region indicates uniform growth under strain-balancing, the red region exceeds the mechanical-equilibrium theory where an increase in dislocation density is expected [19].

Figure 3 is obtained by solving the recurrent equation (5) of M&B using the InP substrate as the unstrained lattice constant. According to the M&B model, 5.04 ML of InAs can be uniformly grown on an InP substrate before strain relaxation occurs through misfit dislocations. The InGaAs critical thickness is plotted varying the In molar fraction x and the region of defect-free coherent growth is represented in green in Figure 3 [22]. The yellow regions are then obtained adding the critical

thickness of a single tensile AlAs barrier of varying thickness, the InGaAs introduces a compressive stress that can be compensated by the tensile AlAs. The worst-case scenario is assumed where only the first barrier matters in the relaxation scheme. The red zone will thus exceed this limitation, where growth may be possible, with the risk of introducing increasing numbers of defects.

The dots of Figure 3 indicate the position of the analysed structures on the graph and both are in the yellow region. Sample-B is close to the limit indicated by the 4ML barrier line, but this limit is exceeded if we consider the +1ML fluctuation.
During the growth process, the InGaAs is deposited on the first AlAs barrier, this barrier alone has to balance the QW 16-ML stress until the second barrier is complete, for highly-mismatched design, imperfections are more likely to occur [23, 24]. This relative thick stack of MLs is more exposed to strain-induced relaxation due to nucleation of dislocation [25] leading to the formation of islands [26, 27].

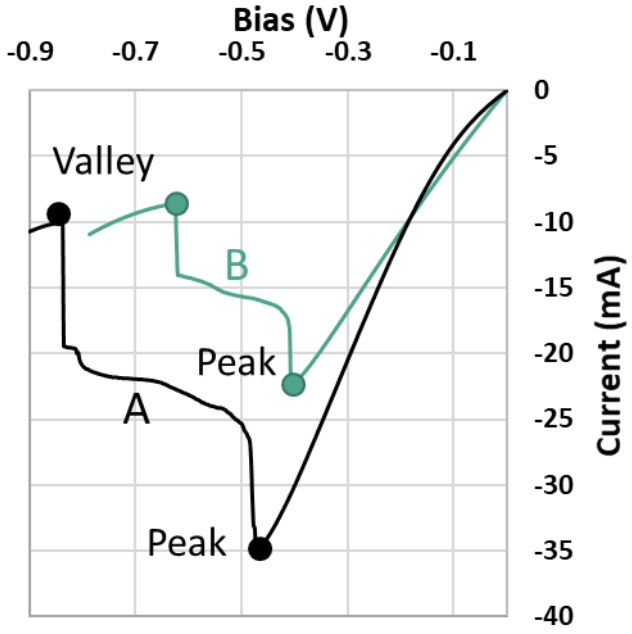

Figure 4 Measured I-V characteristics from sample A (Black) and sample B(Green).

Figure4 plots the I-V characteristics obtained from sample-A&B with an RTD mesa area of 2.4 μm^2. Devices were fabricated in the same fabrication run under the same conditions. Details about the fabrication process are reported elsewhere [18]. Measurements were conducted in the third quadrant to minimize self-heating and prevent catastrophic failure [7]. The peak and valley voltages and currents are indicated. Device performance are in line with our previous predictions. Sample-A shows the highest current peak and higher intrinsic resonator efficiency [21], the narrow well reduces the electron transit time increasing the peak current. The resonant condition is reached faster in sample B thanks to the wider well that moves the first quasi-bound states to lower energy, in sample-A the effect of a narrow well is partially compensated with an higher molar fraction that reduces the e_1 and increases the e_2 level. As a consequence, the peak voltage is similar to sample-B while the valley voltage is increased, improving the ΔV. Despite the difference in the peak current, samples show a similar valley current for this device.

We have shown that PL mapping using a ~100-300 μm^2 excitation area [28] of the entire wafer surface showed a uniform spectral response for both designs, confirming uniform macroscopic properties. However, for high-current-density THz RTDs, much smaller regions of the sample are scanned.

Figure 5(a) plots the peak and valley currents of three device fabrication runs from sample A with mesa areas of 1.2, 1.4, 1.6, 1.8, 2.0, 2.4, and 3 μm^2. Larger area test devices were shown to exhibit catastrophic failure. Figure 5(b) plots the same data for three device fabrication runs from sample B. For sample A, we observe a monotonic increase in both peak and valley current increasing the mesa area. For sample B, whilst the peak current increases in a monotonic correlation, the valley current varies significantly, with only a collective increasing trend being observed in increasing the device area The variation between device fabrication runs is also significant. Barrier and well heterointerface roughness has been shown to increase valley current due to electron scattering [29]. Using a step-by-step procedure of I-V measurement and etching we previously demonstrated how the structural imperfections have a strong impact on the RTD valley current [7].

Variation in the valley current characteristics are significant in sample-B, showing poor area scalability and reproducibility as compared to sample-A. Variations in the valley current are often attributed to errors in the fabrication process in the canon. However, our samples were fabricated side-by-side in multiple processing runs, where such errors would be detected early. We note the observation in valley current variation is consistent with the micro-PL data in Figure 2, where limited variation in the PL spectrum is observed for sample-A, and significant variations for sample-B. Differences in the RTD characteristics due to island formation growth have been demonstrated in large area devices through variations in charge accumulation, observed by combining PL and I-V measurement [30]. Similar to a macro-PL scan, large devices are expected to cover multiple ML islands, and the I-V characteristic are obtained from the average electronic properties of the device area. By contrast, our comparatively small devices were fabricated on an area that is of a similar scale to a single ML island (XML, +1ML, -1ML) or parts thereof. Consequently, the local electronic properties may be expected to be different, affecting the valley current and consequently the scaling and reproducibility of the valley current.

We therefore note that in tackling the challenge of reducing the valley current in high-J RTDs for THz applications, the effect of long-range disorder in the epitaxial material requires removal, with micro-PL allowing a route to understanding its effect on valley current.

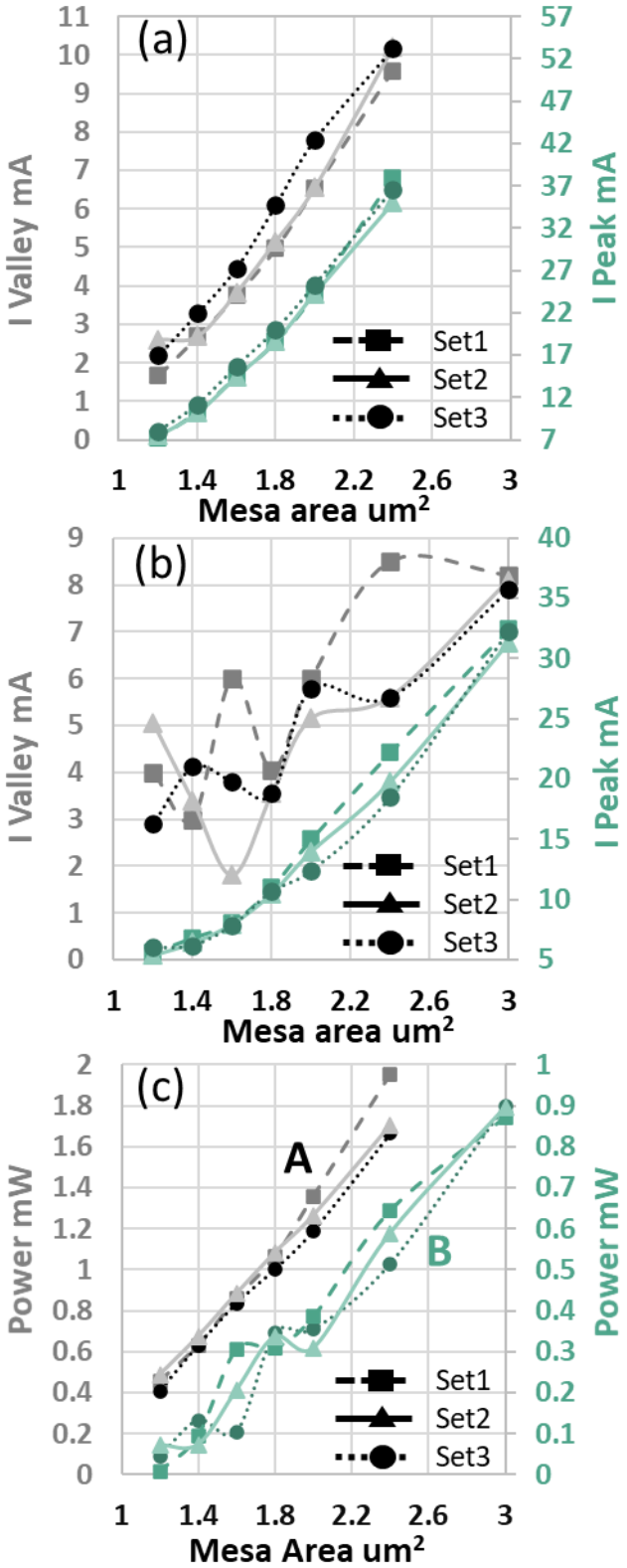

Figure 5 Peak (green) and valley (grey) currents varying the RTD mesa area for 3 different device fabrication runs. (a) data for sample-A (b) data for sample-B, (c) max output power from sample-A (grey) and sample-B (green). Data-sets indicated by markers (square, triangle, and dot). Lines as a guide for the eye.

Figure 5c shows the theoretical maximum RF power $P_{RF,max} \approx \frac{3}{16}\Delta I \Delta V = \frac{3}{16} A \Delta J \Delta V$ [31] of the measured RTD devices as a function of the associated mesa area of sample-A&B, respectively.

As plotted in figure 5c, a linear trend characterises sample-A, meaning that both the available current density *ΔJ* and voltage swing *ΔV* of the devices are the same. Moreover, the difference between the three sets of devices is negligible, indicating wafer structural uniformity and high yield.

On the other hand, sample-B presents a highly non-linear oscillatory behaviour due to the associated instability of the valley current and so *ΔJ*, which is caused by monolayers fluctuations in the QW and islands formation as previously discussed. In addition, the three sets of devices do not present the same trend. This is detrimental in terms of oscillator performance since the major contribute to the RF power of high-current density RTDs is provided by *ΔJ*, whose unpredictability and associated low reproducibility level inevitably leads to a large statistical deviation of output power performance.

We have reported the application of micro-PL to understand micro-scale uniformity of high-J InGaAs/AlAs/InP RTD structures for THz applications, not observable through standard macro-scale PL. Two similar samples are shown to exhibit different long-range disorders through the variation of their PL lineshapes with reducing excitation/detection area. Devices fabricated from these materials show poor valley current scaling and reproducibility suggesting that the material variation is a critical factor in the device performance. The need for such characterisation techniques to cast a light on material uniformity, and future device design and epitaxial process development to minimise the valley current is highlighted.

Acknowledgments
This project has received funding from the European Union's Horizon 2020 research and innovation programme under the Marie Skłodowska-Curie grant agreement No 765426 (TeraApps).

Data availability statement
The data that support the findings of this study are available from the corresponding author upon reasonable request.

References

1. H. Elayan, IEEE Open Journal of the Communications Society **1**, 1 (2019)
2. S. Cherry, IEEE Spectrum **41**, 58 (2004).
3. T. Nagatsuma, IEICE Electron. Express **8**, 1127 (2011).
4. R. Izumi, S. Suzuki, and M. Asada, in 42nd International Conference on Infrared, Millimeter, and Terahertz Waves (IRMMW-THz) (2017).
5. S. Suzuki, M. Asada, A. Teranishi, H. Sugiyama, and H. Yokoyama, Applied Physics Letters, **97**, 242102 (2010)
6. A.E. Yachmenev, S. S. Pushkarev, R. R. Reznik, R. A Khabibullin, and D. S. Ponomarev,. Progress in Crystal Growth and Characterization of Materials, 100485 (2020)
7. K. J. P. Jacobs, B. J. Stevens, R. Baba, O. Wada, T. Mukai, and R. A. Hogg, AIP Advances, **7** 105316 (2017)

8. R. Baba, K. J. P. Jacobs, B. A. Harrison, B. J. Stevens, and T. Mukai, and R. A. Hogg, J. Appl. Phys. **126**, 124304 (2019).
9. K. J. P. Jacobs, B. J. Stevens, and R. A. Hogg, IEICE Trans. Electron. **E99.C**, 181 (2016).
10. M. Cito, O. Kojima, B. J. Stevens, T. Mukai, and R. A. Hogg, AIP Advances, **11** 035122 (2021)
11. M. Cito, O. Kojima, B. J. Stevens, T. Mukai, and R. A. Hogg Proceding of SPIE International Society for Optics and Photonics. *(*2021)
12. M. J. S. P. Brasil, R. E. Nahory, M. C. Tamargo, and S. A Schwarz, Applied physics letters, **63** 2688 (1993)
13. Herman, M., D. Bimberg, and J. Christen, Journal of Applied Physics, **70** 1 (1991)
14. Christen, J., M. Grundmann, and D. Bimberg, Journal of Vacuum Science & Technology B: Microelectronics and Nanometer Structures Processing, Measurement, and Phenomena, **9** 2358 (1991)
15. L. Porte, Journal of crystal growth, **273** 136 (2004)
16. H. Sugiyama, Japanese journal of applied physics, **44** 7314 (2005)
17. J. Wang, K. Alharbi, A.Ofiare, H. Zhou, A. Khalid, D. Cumming, , and E. Wasige, *IEEE Compound Semiconductor Integrated Circuit Symposium (CSICS) 1* (2015)
18. K.J.P Jacobs, B. J.Stevens, O. Wada, T. Mukai, D. Ohnishi, and R. A. Hogg, IEEE Electron Device Letters, **36** 1295 (2015)
19. Matthews, J. and A. Blakeslee, Journal of Crystal growth, **27** 118 (1974)
20. S. Jain, , M. Willander, and H. Maes,. Semiconductor science and technology **11** 641 (1996)
21. R. Baba, B. J. Stevens, T. Mukai, and R. A. Hogg, IEEE Journal of Quantum Electronics, **54** 1 (2018)
22. K.J. Jacobs, *41st International Conference on Infrared, Millimeter, and Terahertz waves (IRMMW-THz) (2016)*
23. N. Ekins-Daukes, K. Kawaguchi, and J. Zhang, Crystal Growth & Design, **2** 287 (2002)
24. Y. Tu, and J. Tersoff, Physical review letters,. **93** 216101 (2004)
25. Tersoff, J. and F. LeGoues, Physical review letters, **72** (1994)
26. Eaglesham, D. and M. Cerullo, Physical review letters, **64** 1943 (1990)
27. Y. Nabetani, N. Yamamoto, T. Tokuda, and A. Sasaki, **146** 363 (1995)
28. K. Jacobs, B. J. Stevens, T. Mukai, D. Ohnishi, and R. A. Hogg, Journal of Crystal Growth, **418** 102 (2015)
29. J.D. Bruno, and J. Hurley, Superlattices and microstructures, **11** 23 (1992)
30. Y.G. Gobato, A. L. C. Triques, P. H. Rivera, and P. A. Schulz, Physical Review B **60** 5664 (1999)
31. C. Kim, and A. Brandli, IRE Transactions on Circuit Theory, **8** 416 (1961)